Observation of a highly conductive warm dense state of water with ultrafast pump-probe free-electron-laser measurements

Z. Chen,[1, a)] X. Na,[1] C. B. Curry,[1, 2] S. Liang,[1] M. French,[3] A. Descamps,[1, 4] D. P. DePonte,[1] J. D. Koralek,[1] J. B. Kim,[1] S. Lebovitz,[1, 5] M. Nakatsutsumi,[6] B. K. Ofori-Okai,[1] R. Redmer,[3] C. Roedel,[7, 8] M. Schörner,[3] S. Skruszewicz,[9] P. Sperling,[6] S. Toleikis,[9] M. Z. Mo,[1] and S. H. Glenzer[1, b)]

[1)]*SLAC National Accelerator Laboratory, Menlo Park, California 94025, USA*

[2)]*University of Alberta, Edmonton, Alberta T6G 1H9, Canada*

[3)]*University of Rostock, Institute of Physics, D-18051 Rostock, Germany*

[4)]*Aeronautics and Astronautics Department, Stanford University, Stanford, California, 94305, USA*

[5)]*Northwestern University, Evanston, Illinois 60208, USA*

[6)]*European XFEL, 22869 Schenefeld, Germany*

[7)]*Friedrich Schiller University Jena, 07743 Jena, Germany*

[8)]*Technical University Darmstadt, 64289 Darmstadt, Germany*

[9)]*Deutsches Elektronen-Synchrotron DESY, 22607 Hamburg, Germany*

The electrical conductivity of water under extreme temperatures and densities plays a central role in modeling planetary magnetic fields. Experimental data are vital to test the theories of high energy density water and assess the possible development and presence of extraterrestrial life. These states are also important in biology and chemistry studies when specimens in water are confined and excited using ultrafast optical or free-electron lasers (FEL). Here we utilize femtosecond optical lasers to measure the transient reflection and transmission of ultra-thin water sheet samples uniformly heated by 5.5 nm FEL approaching a highly conducting state at electron temperatures exceeding 20,000 K. The experiment probes the trajectory of water through the high-energy density phase space and provides insights into the changes of the index of refraction, the charge carrier densities, and the AC electrical conductivity at optical frequencies. At excitation energy densities exceeding 10 MJ/kg, the index of refraction falls to $n = 0.7$, and the thermally excited free carrier density reaches $n_e = 5\times10^{27}$ m^{-3}, over an order of magnitude higher than the electrons carriers produced by direct photo-ionization. Significant specular reflection is observed due to the critical electron density shielding of electromagnetic waves. The measured optical conductivity reaches 2×10^4 S/m, a value that is one to two orders of magnitude lower than simple metals in a liquid state. At electron temperatures below 15,000 K, the experimental results agree well with the theoretical calculations using density-functional-theory molecular-dynamics simulations. With increasing temperature the electron density increases and the system approaches as Fermi distribution. In this regime the conductivities agree better with predictions from the Ziman theory of liquid metals.

I. INTRODUCTION

Water has been extensively studied because of its ubiquity and importance for a variety of fundamental processes and technologies. In its liquid phase, water exhibits many thermodynamic anomalies that originate from its well-connected hydrogen bond network [1–3]. Water not only plays a prominent role as solvent in chemistry and biology studies, [4,5] but it is also used as reactant for energy research and technology[6]. Further, water is a key ingredient for many cosmic and planetary processes[7]. For instance, water and water-ice mixtures are highly abundant in ice giant planets such as Uranus or Neptune [8–10]. The high-pressure and -temperature at the core of these planets can create diamond from methane [11], and the polymorphs of water in such conditions might become conductors capable of generating magnetic fields[12,13].

Yet, our understanding on the fundamental properties of water remains limited. One key challenge is the accurate determination of its electrical conductivity in the so-called warm dense matter (WDM) regime that typically spans eV temperatures at near solid densities[14–16]. On one hand, this is driven by its practical importance to understand planetary processes such as the generation of the magnetic fields in Uranus or Neptune[12,13,17]. A representative example falling into this category is the recent measurement of the optical reflection of shock-compressed water[18–20]. Characteristic changes in reflectivity and electrical conductivity indicated the existence of superionic water ice at planetary interior conditions [21].

On the other hand, water in extreme conditions[22] is also important to a vast number of X-ray Free Electron Lasers (XFELs) experiments for physics [23], chemistry[24] and biology studies[25], where the interaction of short and intense XFELs will lead to warm dense conditions. Further, the transport properties of warm dense water plays a crucial role in evaluating the sample environments and their effect on the dynamics under study. In particular, the electrical conductivity is determined by the mobile-electron density, ionic structure, and the interaction between the electrons and ions[26]. An intense XFEL can excite an enormous number of electrons, modifying the potential landscapes of the electrons and ions. While there has been experimental effort to understand its structural properties using the X-ray diffraction technique[27], the measurement of the electrical conductivity of water under well characterized warm dense matter conditions is still lacking.

To determine the electrical conductivity of warm dense matter, it routinely requires the measurements of optical re-

[a)]Electronic mail: zchen@slac.stanford.edu

[b)]Electronic mail: glenzer@slac.stanford.edu

flection and transmission of the excited samples [28–30]. The AC electrical conductivity at the frequency of the optical probe pulse is deduced accordingly. These measurements require the sample surface to be optically flat. The recent development of gas-dynamic liquid nozzles demonstrates the delivery of these liquid samples with sub-micrometer thickness[31]. It opens a unique avenue to study the electrical conductivity of XFEL excited warm dense water at high-repetition-rate. Here, we achieve a warm dense state of water by irradiating an ultrathin water sheet jet with λ =13.6 nm radiation produced by an FEL at 10 Hz, reaching electron temperatures in the range of 10,000 K to 20,000 K and the mass density of ambient liquid water.

The AC electrical conductivity was determined from the simultaneous measurement of the optical reflection and transmission of ultrafast probe pulses at two different wavelengths, i.e. 750 nm and 850 nm. Since the photon energies of these two probe wavelengths are below the bandgap between the highest occupied molecular orbital (HOMO) and the lowest unoccupied molecular orbital (LUMO) of water as well as below the vertical binding energy of solvated electrons in water[32], we expect the measured conductivity to be dominated by the contributions from the electrons in the conduction band of the excited water.

At the highest excitation energy densities, we observed that the index of refraction falls to n = 0.7, and the free carrier density exceeds $n_e = 10^{27}$ m^{-3}, which is much higher than the density estimated by direct photo-ionization and is believed to be the result of carrier multiplication during thermalization of excited electrons. Further, the heated samples reach an optical conductivity of up to 2×10^4 S/m, within 2 orders of magnitude of the values in liquid phase simple metals[33]. In parallel, the samples become reflective and show shielding of the laser light. At moderate temperatures, the experimental results agree well with theoretical calculations using density-functional theory molecular dynamics (DFT-MD)[13]. At temperatures exceeding 15,000 K, the measurements agree better with the predictions from Ziman theory [34], which is a manifestation of the liquid-metal-like electrical properties.

II. EXPERIMENT

The experiment was carried out in the BL3 end-station of the Free-electron LASer in Hamburg (FLASH) facility at Deutsches Elektronen-SYnchrotron (DESY). We utilized 225 eV extreme ultraviolet (XUV) FEL pulses to excite and heat the free-standing water sheet-jet samples to a maximum energy density of 12 MJ/kg. The specular reflection and transmission of the excited water were measured simultaneously as a function of the pump-probe delay time for two individual optical wavelengths to determine the complex reflective index and the optical conductivity of the excited water. Detailed descriptions of our experiment are given below.

A. Experimental setup and data acquisition

The free-standing ultrathin water samples were delivered by a microfluidic gas-dynamic nozzle; the details of the system are described elsewhere[31]. In brief, the ultra-pure liquid water (HPLC Plus grade, Sigma-Aldrich) is accelerated and flattened by pressurized helium gas, forming an optically flat water leaf 300 µm in height and 80 µm in width right below the nozzle exit. The thickness of the water leaf varies from $\sim$ 1 µm at the nozzle exit position to less than 100 nm at the other end of the leaf. The sample thickness as a function of position is determined from the thin film interferometry on the reflection images. Instead of using a white light source to form color fringes [31], the constructive and destructive fringes from the probe pulses are applied for *in situ* measurements. The interference pattern as a function of thickness is calculated according to the textbook [35]. Because the film thickness increases continuously from the bottom to the top of the water leaf [31], we first identified the first constructive fringe from the bottom and use it as a reference point to determine the thickness at different positions based on the local reflectivity.

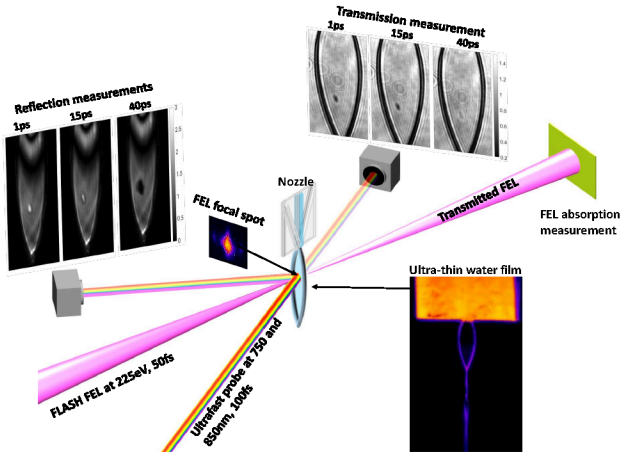

FIG. 1. Schematic diagram of the experimental setup. Optically smooth water thin film is generated from a gas-dynamic liquid nozzle. The thin film is heated by the FLASH XUV-FEL focused by an ellipsoidal mirror to 45 µm$\times$ 24 µm FWHM. The transmitted ratio of the FEL energy is measured by a YAG screen. The optical reflection and transmission of the thin film sample are probed by 750 nm and 850 nm, 100 fs FWHM laser pulses generated from an optical parametric amplifier. The measurement is carried out continuously at 10 Hz. Example reflection and transmission data measured by 850 nm probe at energy density of 9.1$\pm$1.2 MJ/kg are shown.

Figure 1 shows a schematic diagram of the experimental setup. The FEL pulses excited the sample at normal incidence. The FEL pulse energies were measured by online gas-monitor detectors (GMD) and varied in the range of 10 – 50 µJ during the measurements. The FEL pulse duration was shorter than 50 fs full width half maximum (FWHM).[36] The FEL pulses were relayed into the sample chamber through grazing angle reflections from carbon and nickle-coated mirrors that have a combined efficiency of $\sim$ 63%. These FEL pulses were then focused onto the sample surface by an ellipsoidal mirror with

a focal length f = 2 m and a reflectivity of 84% at 225 eV.[36] The focal spot was measured to have an elliptical profile with FWHM dimensions of 45 µm (vertical) × 24 µm (horizontal). The FEL was operated at a repetition rate of 10 Hz, which provided sufficient time between shots for the water leaf to replenish itself. This ensured that each pump-probe measurement in our experiment was carried out on a fresh water sample. The absorption of the FEL pulses was measured by a YAG screen-based detector that was located 1 m after the sample. By monitoring the FEL-induced fluorescence intensity on a YAG screen with and without the water sample, we find that the XUV transmission through 200 nm and 300 nm-thick water are $(82.2 \pm 2.6)\%$ and $(77.4 \pm 2.7)\%$, which are in close agreement with the predictions of 83.1% and 75.9% according to the well-known XUV transmission model [37]. Because of these high transmission ratios, the FEL energy deposition can be considered to be uniform along the propagation direction inside the sample. This allows us to calculate the absorbed energy density ΔE from the FEL fluence via the expression: $\Delta E = \alpha F/d$, where α is the FEL absorption ratio, F is the incident FEL fluence, and d is the sample thickness.

Time-resolved reflectivity and transmissivity measurements of the excited water were measured using 100 fs FWHM laser light at wavelengths of 750 nm and 850 nm. Probe pulses were generated from an optical parametric amplifier (OPA) that was driven by 800 nm, 60 fs pulses from a Ti:Sapphire laser system. Due to the non-linear frequency conversion in the OPA system, the pre- and post-pulses of the fundamental laser pulses are improved. These probe beams were collimated by a 1 mm diameter iris that was 2 m upstream from the sample, so that the full water leaf can be uniformly illuminated and imaged. In both cases the probe laser was S-polarized and the incident on the sample at an angle of 22.5°. The reflection and transmission images of the the water leaf were recorded on two cameras. The time-resolved measurements were scanned from -2 ps to 50 ps after the excitation. The step size was 0.1 ps from -2 ps to 5 ps, and after 5 ps, the step size was increased to 1 ps, with 100 measurements collected at each time step.

B. Analysis of the probe beam reflection and transmission

For each probe wavelength, over 10,000 data shots were collected over the entire time scan. In order to compensate for the shot-to-shot fluctuations of the FEL, the energy of each FEL pulse recorded by GMD was used to group the acquired data within a range of ±2.5 µJ (e.g. 10 ± 2.5 µJ). Between 1000 – 2000 independent measurements were analyzed in each pulse energy range. The reflection, R, and transmission, T, ratio values of the heated samples are derived from the recorded images. On each image, R and T were determined by comparing the relative brightness of the heated region with several reference regions. An example of data analysis is shown in Fig. 2.

In the reflection image (Fig. 2(a)), the curved thin-film interference pattern resulting from a gradient in jet thickness was flattened using a cross-correlation method as shown in the figure. The averaged pixel count in the FEL-heated region (6 × 6 pixels in the ROI) was normalized to the the maximum and minimum intensities of the thin film interference pattern. The absolute reflectivity was determined as,

$$R = R_{peak} \cdot \frac{I_R^{FEL} - I_R^{min}}{I_R^{max} - I_R^{min}}, \quad (1)$$

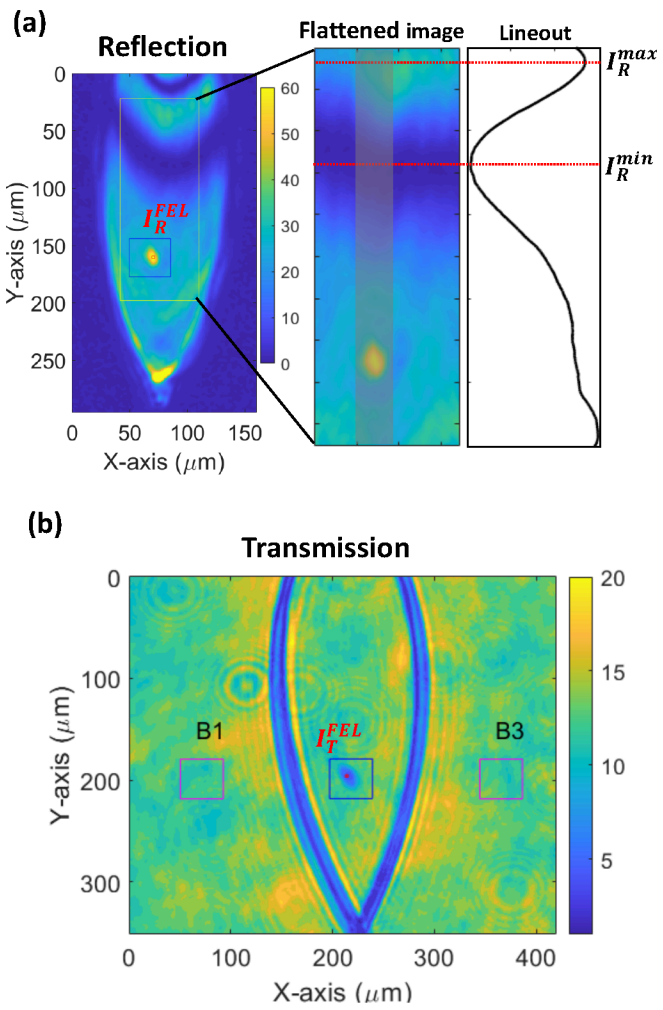

FIG. 2. Examples of the reflection and transmission data analysis. The data are acquired using 850 nm probe at 300 fs after the FEL excitation. (a) The raw reflection image on the left contains curved interference fringes, and the FEL heated region is marked by a blue box. The average counts at the center of the FEL heated area (small red dot) is used as I_R^{FEL} in Eq. 1. The fringes inside the yellow box are flattened by a cross-correlation function and the result is showed in the middle. The lineout taken from the flattened image is shown on the right, where I_R^{max} and I_R^{min} are obtained for Eq. 1. The grey box in the flattened image containing the FEL heated region is excluded when we calculate the lineout curve. (b) The center of the FEL heated region (small red dot) in the raw transmission image is used to determined I_T^{FEL} in Eq. 2. The vacuum area in boxes B1 and B3 are used to determine the reference vacuum transmission I_T^v in the same equation. The distance from B1 and B3 to the FEL heating spot are the same.

where $R_{peak} = 0.0965$ is the peak reflectivity due to the thin film interference [35], I_R^{FEL} is the average intensity in counts on the detector in the FEL-heated area, and I_R^{max} and I_R^{min} are the maximum and minimum intensity on the detector along the interference pattern, respectively. All these values are determined on the same image so that the shot-to-shot fluctuations of the probe pulse intensity are corrected.

In the transmission image (Fig. 2 (b)), the pixel counts in the FEL heated region are normalized to areas without sample, where 100% transmission is expected. The absolute transmission is obtained by,

$$T = \frac{I_T^{FEL}}{I_T^v} \cdot C_{Norm}, \tag{2}$$

where I_T^{FEL} and I_T^v denote the average counts in the area of FEL heating and without sample, and C_{Norm} is a normalization factor to compensate for the spatial heterogeneity of the probe and is determined from the data before FEL heating by the requirement that $R+T=1$ when $t <$ -0.1 ps. We set $I_T^v = (I_T^{B1} + I_T^{B3})/2$ to balance the vacuum transmission on both sides of the water sample.

The time-dependent reflection and transmission at different excitation energy densities measured by the 750 nm and 850 nm probe pulses are shown in Fig. 3. Immediately after the XUV-FEL heating, we observe a sharp increase in the reflectivity and a rapid decrease of transmission. These two effects result from the generation of conduction electrons. Initially, water molecules are ionized by absorption of XUV photons. However, the inelastic mean free path of 200 eV electrons in water is about 1 nm [38]. Thus, the electrons collide with neighboring water molecules, transfer their energy, and promote the electrons into the conduction band. The high density of excited electrons screen the electric field of the probe pulse, causing an increase in reflection and decrease of transmission. At the same time, the excess electrons absorb energy, some of which is lost through collisions consistent with Ohm's law[26], resulting in $R+T<1$. At higher excitation energy densities we observe higher reflectivity and lower transmission, consistent with the increased creation of free carriers.

The substantial increase in reflectivity indicates that the free electron density in the heated water is comparable to the critical densities of the probe pulse wavelengths, i.e., 2×10^{27} m^{-3} and 1.5×10^{27} m^{-3} for 750 nm and 850 nm photons, respectively. At an excitation energy density of 10 MJ/kg, we calculate that the number density of electrons created by the absorption of 225 eV photons is only 2.8×10^{26}/m^3.

Shortly after the reflection reaches the peak values, we find that it quickly drops to nearly zero in a significant shorter time than the corresponding transmission data (>50ps). The latter indicates that the electron-ion equilibrium time is much slower than for XUV-FEL heated hydrogen in similar temperature conditions (2-3ps).[39,40]. This is expected because the water molecules are much heavier than hydrogen. Further, the fast disappearance of the reflection is likely due to the formation of gradients on the sample surfaces [41,42]. The smearing of the vacuum-water interface suppresses the reflection [43], but the absorption of the probe pulse is not affected. In the following sections, we only focus on early-time data (<5 ps) before the gradient effects become significant.

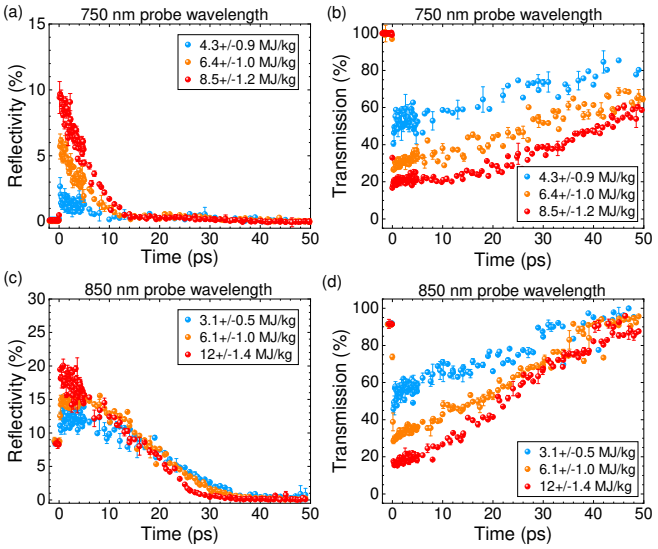

FIG. 3. Measured reflection and transmission data. (a) and (b) are the data for a (300 ± 30) nm thin water film heated to various energy densities and measured by 750 nm probe. (c) and (d) are the data of (200 ± 20) nm thin film measured by 850 nm probe. The initial reflectivity in the 850 nm data is significantly higher than the 750 nm data. This is because the 850 nm measurements were carried out near the peak intensity of the interference fringes, while 750 nm measurements were near the minimum intensity of the fringes.

C. Refractive index and conductivity determined from the experimental data

The reflectivity and transmissivity of an isotropic thin film are dictated by its refractive index, sample thickness, and the polarization, incident angle, and wavelength of the probe beam. To determine the refractive index for our experimental data, we first use the transfer-matrix method[29,35] to calculate the corresponding reflection and transmission in 200 nm- and 300 nm-thick films over a wide range of refractive indices. Subsequently, we find the refractive indices that produce the reflection and transmission matching best with our measurements. Examples for the measurements using 750 nm and 850 nm probes are shown in Figs. 4 and 5, respectively, where (c) and (d) in each figure show the real and imaginary parts of the reflective index (n and k) as a function of delay time that corresponds to the measured data in (a) and (b). The time step interval is 0.1 ps before 5 ps, and it increases to 1 ps at later time delay. About 10-20 individual data points were measured at each time step. The data points and the error bars represent the mean values and the standard deviations of the data measured at each time delay. In general, we find that n decreases from 1.33 to less than 1, a value that is characteristic of a plasma state. Simultaneously, k increases from zero to some fraction of unity. This high value of k indicates strong light absorption that is consistent with $R+T<1$ after the FEL

heating.

Figures 4 (e) and (f) [5 (e) and (f)] show the real part and imaginary part of the inferred optical conductivity σ, respectively, for the 750 nm [850 nm] probe. The optical conductivity is a function of the complex refractive index and is given by [26] :

$$\sigma = i \cdot (1 - (n + ik)^2)\varepsilon_0 \omega, \tag{3}$$

where ε_0 is the permittivity of free space, and ω is the oscillation frequency of the probe beam. The square of refractive index, i.e. $(n+ik)^2$, is equivalent to the complex dielectric function. The initial value of σ_r=0 and $\sigma_i < 0$ at room temperature corresponds to typical dielectric material. Upon FEL heating, we can see that both the real and imaginary parts increase to the order of 10^4 S/m. The trajectories of the measured reflection and transmission and the determined conductivity as functions of absorbed FEL energy density are shown in Fig. 6 (a) and (b) [(c) and (d)] for 750 nm [850 nm] probe pulse. Near the trajectories of the heated samples, the contour lines in reflection are close to parallel to the vertical axis, indicating that the reflection is less sensitive to the change of σ_r than σ_i in our experimental conditions. On the other hand, the transmission data is sensitive to both σ_r and σ_i. The increase of σ_r indicates the rise conduction electron density that enhances both the plasma shielding and reflection, however the higher σ_r also enhances the absorption of electromagnetic wave within the material[44] and attenuates the reflection. The competition of both effects therefore makes the reflection of the probe pulses less sensitive to σ_r.

III. THEORETICAL CALCULATIONS

To gain more insight to our experimental results, we performed two different theoretical methods to calculate the electrical conductivity of the XUV-FEL heated warm dense water. The first method implements the Kubo-Greenwood formalism based on the density-functional-theory coupled with molecular-dynamics simulations (DFT-MD) [45]. The other method makes use of Ziman theory [34] of electrical conductivity based on the estimation of electron density from DFT-MD and the total ionic structure factor computed from classical MD simulations [46].

A. Density Functional Theory - Molecular Dynamics Simulations

We performed DFT-MD simulations for water at the 1 g cm^{-3} isochore with the Vienna Ab initio Simulation Package (VASP) [47–50] using 54 molecules and the PBE [15,51] functional, similar as in earlier work[52,53]. To describe the ultrafast FEL experiment, we ran two-temperature simulations with a constant ionic temperature of T_i = 300 K and varied the electronic temperature between 300 and 40,000 K. From the DFT-MD simulations we obtained the isochoric heat capacity C_e of the electrons by numerical differentiation of the internal energy as shown in Fig. 7(a). Subsequently, the relation between the peak electron temperature and the absorbed FEL energy density, ΔE, is,

$$\Delta E = \int_{300\ K}^{T_e^{peak}} C_e(T_e)\, dT_e. \tag{4}$$

It is worth noting that we assume all of the absorbed energy remains in the electron system within the first half picosecond after FEL heated. This assumption is supported by the long time scales of the measured reflection and transmission, which suggests that the electron-ion energy relaxation time scale is on the order of 10s of picoseconds. Figure 7 (b) shows the result of ΔE versus T_e.

The frequency-dependent conductivity $\sigma_r(\omega)$[45,54] is also calculated via the Kubo-Greenwood formalism[55,56] using ionic configurations of all DFT-MD simulations and the Heyd-Scuseria-Ernzerhof (HSE) functional[57]. The imaginary parts of the conductivity at the probe laser wavelengths of 750 and 850 nm can also be determined using the Kramers-Kronig re-

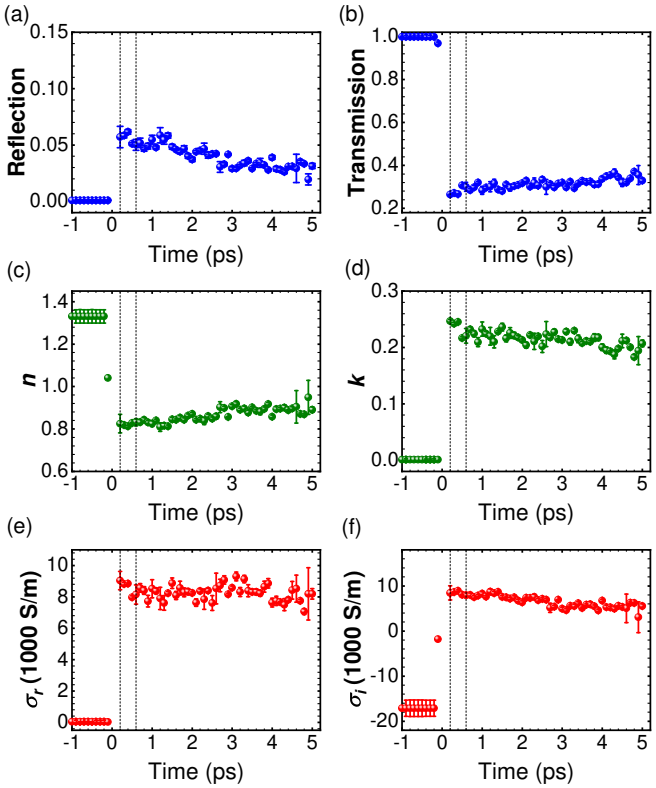

FIG. 4. The 750 nm probe wavelength measured reflection and transmission, and the deduced complex refractive index and optical conductivity of water (300 nm thick) at absorbed energy density of (6.4 ± 1) MJ/kg. (a) and (b) show the averaged reflection and transmission at different time delays; (c) and (d) are the complex refractive index determined from Maxwell's equations implemented by transform matrix method; (e) and (f) are the real and imaginary parts of the corresponding electrical conductivity. The vertical dashed lines indicate the time window of 0.2 – 0.6 ps, where the electrical conductivity is obtained for further discussions.

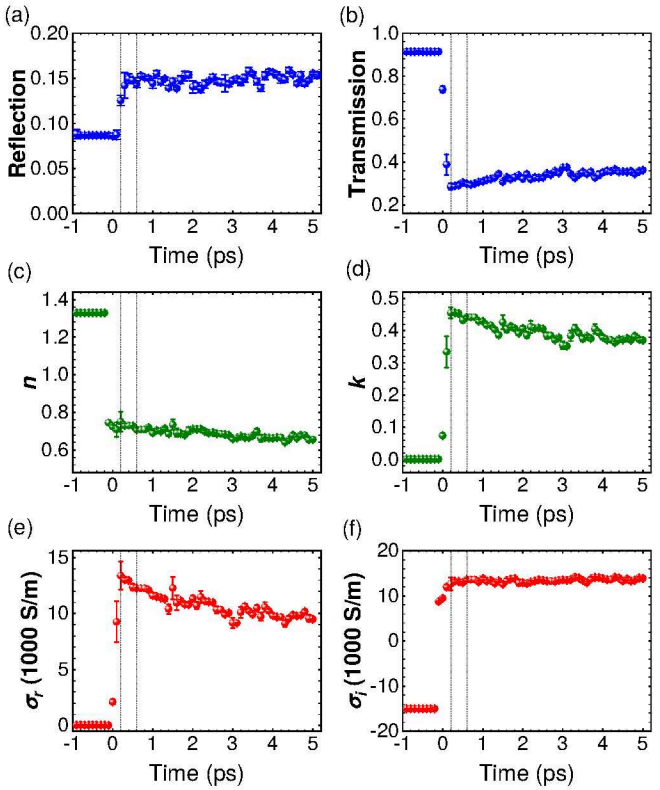

FIG. 5. The 850 nm probe wavelength measured reflection and transmission, and the deduced complex refractive index and optical conductivity of water (200 nm thick) at absorbed energy density of (6.4 ± 1) MJ/kg. (a) and (b) show the averaged reflection and transmission at different time delays; (c) and (d) are the complex refractive index determined from Maxwell's equations implemented by transform matrix method; (e) and (f) are the real and imaginary parts of the corresponding electrical conductivity. The vertical dashed lines indicate a time window of 0.2 – 0.6 ps, where the electrical conductivity is obtained for further discussions.

lations, analogous to the procedure described in Refs. 58 and 59, but it may be less accurate compared to the real part in the warm dense matter regime [29,60].

B. Ziman Theory of Conductivity in the Framework of the Drude Model

The real part of optical conductivity is the sum of free carrier contribution plus the contributions from interband transitions [28]. In the case of water, the photon energy of 750 nm and 850 nm photons is below interband transition energies and is insufficient to ionize conduction electrons to the continuum [32]. Thus, the Drude model is employed to describe the free carrier conductivity[26],

$$\sigma_r = \frac{n_e e^2 \tau}{m_e[1+(\omega\tau)^2]}, \tag{5}$$

where n_e is the carrier electron density, e is the unit charge, m_e is the electron rest mass, τ is the electron relaxation time.

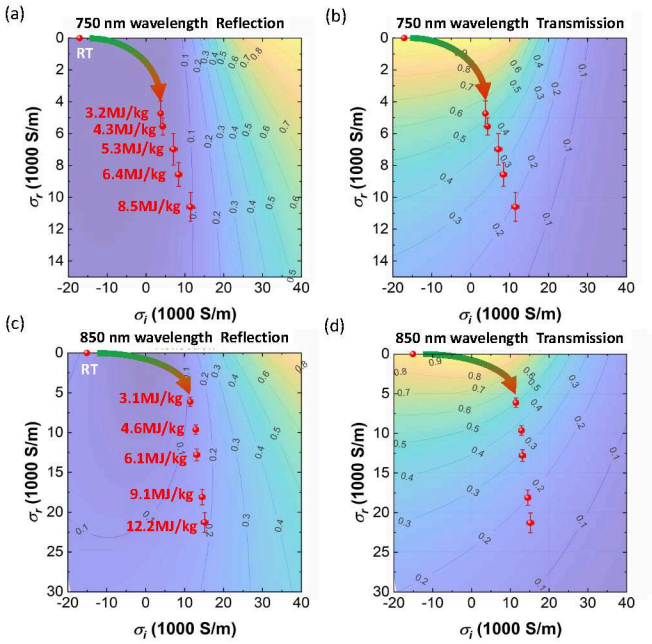

FIG. 6. Real and imaginary parts of the electrical conductivity from cold and heated water (0.2 – 0.6 ps after FEL heating, the error bars represent the standard deviations of the data within this time interval) on the contour plots of reflection and transmission. (a) and (b) show the 750 nm laser probe on 300 nm-thick sample, and the heated states samples are measured at energy densities of (3.2 ± 0.8), (4.3 ± 0.9), (5.3 ± 0.9), (6.4 ± 1) and (8.5 ± 1.2) MJ/kg respectively. (c) and (d) show the 850 nm laser probe 200 nm-thick sample, and the heated states samples are measured at energy densities of (3.1 ± 0.8), (4.6 ± 0.9), (6.1 ± 1), (9.1 ± 1.2) and (12 ± 1.4) MJ/kg respectively. The room temperature data (RT, i.e. $T_e = T_i = 300\ K$) are on the top-left corner in each plot.

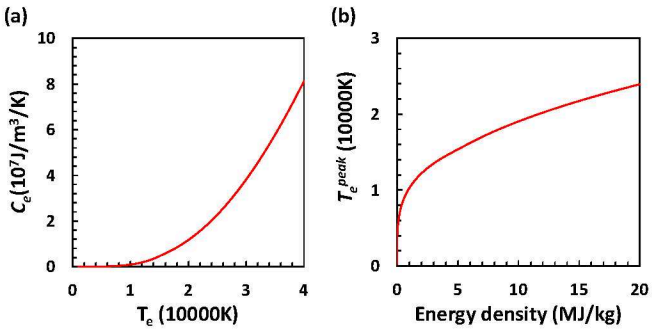

FIG. 7. (a) The electron specific heat capacity as of function of electron temperature from DFT calculations, and (b) the peak electron temperature as a function of absorbed XUV energy density, which is calculated using Eq. 4

The electron density as a function of temperature can be determined from the occupied electron density of states (DOS). We calculated the electronic DOS using the DFT-MD at various electron temperatures. Results for T_e at 300 K and 20,000 K when $T_i = 300$ K are shown in Figs. 8 (a) and (b), respectively. The values of n_e at different electron temperatures, T_e, can be determined by the integral of the Fermi distribution function

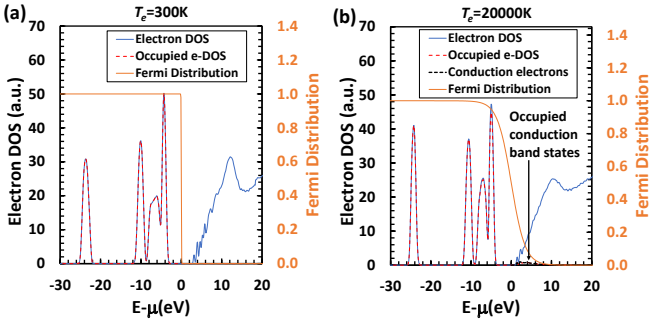

FIG. 8. The electronic density of states of water from DFT calculations at electron temperatures of (a) 300 K and (b) 20,000 K. The ionic temperature is 300 K in both cases.

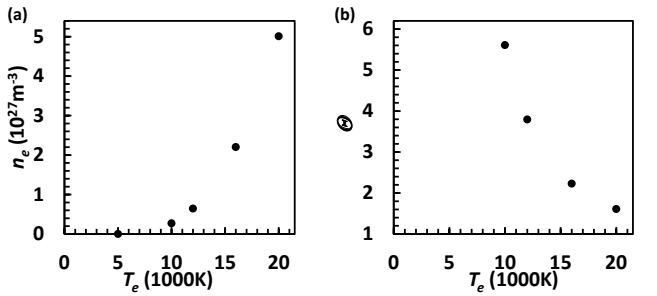

FIG. 9. (a) The density of conduction (carrier) electrons as a function of T_e calculated using the results of the electron density of states and Eq. 6, and (b) the corresponding electron degeneracy parameter (Θ).

$f_{T_e}(E)$ times the e-DOS $g_{T_e}(E)$,

$$n(T_e) = \int_{\mu}^{E_{max}} f_{T_e}(E) g_{T_e}(E)\, dE, \tag{6}$$

where μ is the chemical potential that is determined by the conservation of the total number of valence and conduction electrons[60]. The T_e dependent carrier density is shown in Fig. 9 (a). At $T_e = 5000$ K, n_e is negligible. It starts to increase significantly at higher temperatures, reaching 5×10^{27} m^{-3} at $T_e = 20,000$ K, which corresponds to an absorbed energy density of 11.6 MJ/kg. This electron carrier density equals to 2.5 times of the critical density for 750 nm light, confirming our observed increase of probe beam reflectivity is a result of high density conduction electrons. Fig. 9 (b) shows the electron degeneracy parameter Θ, which is the ratio of thermal energy over the Fermi energy. Because n_e increases rapidly as a function of T_e, the excited electrons become more degenerate at higher temperatures.

The electron relaxation time τ is the inverse number of the scattering frequency υ. We note that υ is very sensitive to changes in temperature and density. For our experimental conditions, the contribution from electron-electron scattering is small because the conduction electron density is still low compared to the atomic density (10^{29} m^{-3}). Thus, υ is dominated by the electron-ion scattering, i.e. $\upsilon \approx \upsilon_{ei}$. The Ziman theory of conductivity enables the determination of υ_{ei} based on the knowledge of the ionic structure factor S_{ii} according to [61],

$$\upsilon_{ei} = \frac{n_i m_e}{2p_F^3} \int_0^{2k_F} \left| \frac{4\pi e^2}{Q^2 + k_e^2} \right|^2 Q^3 S_{ii}(Q) \frac{dQ}{2\pi}, \tag{7}$$

where Q is the momentum transfer vector, k_e is the electron screening vector, which is determined from the electron temperature and density [62], n_i is the molecular density, m_e is the electron rest mass, and k_F and p_F are Fermi wave vector and momentum of the free carriers, respectively.

To estimate S_{ii}, the structure factor of liquid water, classical molecular dynamics simulations were performed at different temperatures under thermal equilibrium condition, i.e: $T_e = T_i$. Here, using classical MD allows us to model a much larger simulation box so that the lower Q range of S_{ii} can be accessed, which is needed to compute υ_{ei} using Eq. 7. The simulation cell contained 1024 water molecules with density ρ = 0.999 g cm^{-3} and was performed under the constant-temperature, constant-volume (NVT) ensemble using the TIP4P/2005 forcefield.[63] At each temperature, the system was equilibrated for 1 ns, and configurations were collected over the following 500 ps. The ion-ion structure factor was computed via:

$$S_{ii}(Q) = \frac{1}{N} \left\langle \sum_{p=1}^{N} \sum_{q=1}^{N} e^{-iQr_{pq}} \right\rangle \tag{8}$$

where Q is truncated at $2\pi/d \approx 0.2$ Å^{-1} with a box size of d = 31.3 Å, and r_{pq} is the distance between the ions p and q.

The S_{ii} results for four different temperatures are shown in Fig. 10. Our result at the room temperature condition is verified with data reported for the O – O structure factor measured by X-ray scattering [64]. The average difference at each Q is calculated to be within 4.6%. As temperature increases, we see that the primary liquid peak moves towards higher Q while its peak height does not seem to significantly change. According to MD simulations, the increase of temperature stretches the correlation peaks in real space, which results in the contraction of the first atomic peak in the total radial distribution function. This is manifested by the primary liquid peak shifting to high Q as observed in Fig. 10.

IV. COMPARISON OF EXPERIMENTAL DATA WITH THEORETICAL CALCULATIONS

Figure 11 shows the comparison of the experimental data at 750 nm and 850 nm with theoretical calculations from the DFT-MD and the Ziman theory. The experimental data at time delays between 0.2 ps and 0.6 ps are averaged. At these time delays, most of the absorbed FEL energy should be in the electronic system while the molecules remain cold. Accordingly, both calculations are carried out using the peak electron temperatures at the corresponding energy densities, Cf. Fig. 9 (a), and ion temperature at 300 K. The σ_r measured from both 750 nm and 850 nm increases as a function of T_e. The

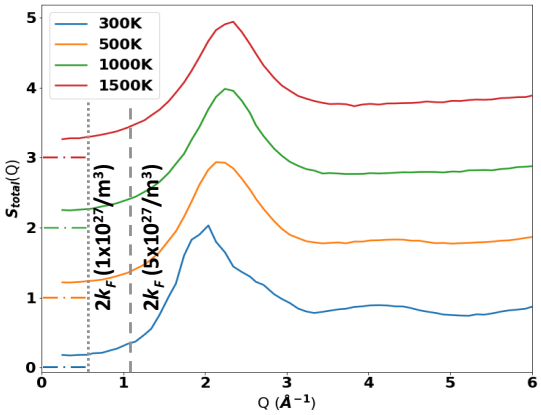

FIG. 10. The total structure factor of water calculated by molecular dynamics simulations at equilibrium temperatures ($T_e = T_i$) of 300 K, 500 K, 1000 K and 1500 K. The baseline of each curve is shown by the dash-dotted lines on the left using the corresponding colors. The vertical dotted line and dashed line correspond to twice the Fermi vector, i.e. the upper bound of the integral in Eq. 7 at carrier densities of 1×10^{27} m^{-3} and 5×10^{27} m^{-3}, respectively.

850 nm conductivity is higher than that at 750 nm. This is a typical Drude-like behavior according to Eq. 5, i.e. σ_r decreases as the frequency of the electric-field ω increases. We observe a similar trend in the theoretical calculations. The DFT-MD calculations agree well with the measurements up to T_e = 15,000 K, especially with the 850 nm data. At higher temperatures, the DFT-MD calculations overestimate the σ_r. On the contrary, the Ziman theory calculations underestimate the results at T_e < 15,000 K, but start to show better agreement at higher temperatures.

The failure of Ziman theory at low temperatures is likely due to the low electron degeneracy in these conditions, i.e. $\Theta \gg 1$ shown in Fig. 9 (b). In this regime, there is no well-defined Fermi surface of the electrons. As the electron temperature increases, the conduction band is populated, Θ approaches unity near T_e = 20,000 K. Consequently, the heated water behaves more like a liquid metal, and its conductivity can be better described by the Ziman theory. Note that as T_i increases, the S_{ii} data below $Q = 2k_F$ also increase as shown in Fig. 10. This will raise υ_{ei} as indicated in Eq. 7. At the same time the conduction band electron density will decrease as energy couples to the ions. These two effects together in turn reduce the magnitude of σ_r, resulting in less agreement with the experimental data, i.e. σ_r will drop by ~20% and ~45% if we assume T_i=500 K and 1,000 K respectively in the Ziman theory calculations. The DFT-MD calculations properly describe the weakly degenerate conditions at low temperatures. However, at this point it is not clear why it does not work at higher temperatures. It is possible that the exchange and correlation functional used in the DFT cannot correctly model the chemical processes in the strongly excited conditions attained in our experiment. Therefore, our measurements provide valuable data to test these theoretical calculations, especially in non-equilibrium states produced by ultrafast laser or FEL excitation, where electron temperature is significantly higher than the ion temperature [29].

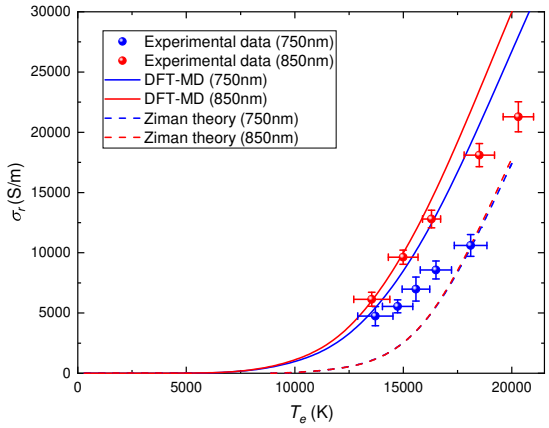

FIG. 11. Optical conductivity as a function of electron temperature T_e. A comparison of the experiments and theoretical calculations. Both DFT-MD and Ziman theory calculations are performed at T_i = 300 K. The error bars in the vertical axis are inherited from Fig. 6, and those in the horizontal axis correspond to the range of energy densities in the data.

V. CONCLUSIONS

Using XUV-FEL pulses to excite optically flat ultra-thin water samples, we have demonstrated the first optical conductivity measurements of isochorically heated warm dense water at a continuous 10 Hz repetition rate. We acquire the conductivity data at the first half picosecond following the FEL excitation, when electron temperatures reach up to 20,000 K while the ions remain cold. The results allow us to test the non-equilibrium calculations using the DFT-MD and Ziman theory. We find that although the DFT-MD calculations can describe the conductivity results at electron temperatures below 15,000 K, further effort is needed to improve its accuracy to predict the conductivity at higher temperatures. Instead, agreement with Ziman theory calculations when T_e approaches 20,000 K is found and indicates that the strongly excited water demonstrates liquid-metal-like behavior when a large number of electrons are excited to the conduction band. Our results bring new insight into a regime of warm dense matter that is relevant for both high energy density physics and ultra-fast chemistry and biology studies. In future studies, we plan to acquire conductivity data with longer time delays so that the samples approach equilibrium conditions. These data could be obtained by transmission ellipsometry or interferometry measurements.

ACKNOWLEDGMENTS

This work was supported by the U.S. Department of Energy, Office of Science, Fusion Energy Science under FWP 100182. C. C. acknowledges partial support from the Natural Sciences and Engineering Research Council of Canada

(NSERC). J.D.K. and D.P.D. are supported by the U.S. Department of Energy, Office of Science, Office of Basic Energy Sciences under Contract No. DE-AC02-76SF00515. M. M. acknowledges partial support from the U.S. Department of Energy, Laboratory Directed Research and Development (LDRD) program at SLAC National Accelerator Laboratory, under contract DE-AC02-76SF00515. M.F. and R.R. thank the Deutsche Forschungsemeinschaft (DFG) for support within the Research Unit FOR 2440. The work of S. L. was supported in part by the U.S. Department of Energy, Office of Science, Office of Workforce Development for Teachers and Scientists (WDTS) under the Science Undergraduate Laboratory Internships (SULI) program. C. R. acknowledges support from the LOEWE excellence initiative of the state of Hessen.

VI. REFERENCES

[1] J. A. Sellberg, C. Huang, T. A. McQueen, N. D. Loh, H. Laksmono, D. Schlesinger, R. G. Sierra, D. Nordlund, C. Y. Hampton, D. Starodub, D. P. DePonte, M. Beye, C. Chen, A. V. Martin, A. Barty, K. T. Wikfeldt, T. M. Weiss, C. Caronna, J. Feldkamp, L. B. Skinner, M. M. Seibert, M. Messerschmidt, G. J. Williams, S. Boutet, L. G. M. Pettersson, M. J. Bogan, and A. Nilsson, "Ultrafast X-ray probing of water structure below the homogeneous ice nucleation temperature." Nature **509**, 381 (2014).

[2] K. H. Kim, S. Kim, J. Park, T. Katayama, K. H. Nam, H. Pathak, F. Perakis, J. H. Lee, A. Späh, J. A. Sellberg, K. Amann-Winkel, D. Mariedahl, and A. Nilsson, "Maxima in the thermodynamic response and correlation functions of deeply supercooled water," Science **358**, 1589 (2017).

[3] K. H. Kim, K. Amann-Winkel, N. Giovambattista, A. Späh, F. Perakis, H. Pathak, M. L. Parada, C. Yang, D. Mariedahl, T. Eklund, T. J. Lane, S. You, S. Jeong, M. Weston, J. H. Lee, I. Eom, M. Kim, J. Park, S. H. Chun, P. H. Poole, and A. Nilsson, "Experimental observation of the liquid-liquid transition in bulk supercooled water under pressure," Science **370**, 978 (2020).

[4] F. Perakis, L. D. Marco, A. Shalit, F. Tang, Z. R. Kann, T. D. Kühne, R. Torre, M. Bonn, and Y. Nagata, "Vibrational Spectroscopy and Dynamics of Water," Chemical Reviews **116**, 7590–7607 (2016).

[5] H.-X. Zhou and X. Pang, "Electrostatic interactions in protein structure, folding, binding, and condensation," Chemical Reviews **118**, 1691–1741 (2018).

[6] V. Maurice and P. Marcus, "Progress in corrosion science at atomic and nanometric scales," Progress in Materials Science **95**, 132 – 171 (2018).

[7] W. B. Hubbard, "Interiors of the giant planets," Science **214**, 145–149 (1981).

[8] R. Redmer, T. R. Mattsson, N. Nettelmann, and M. French, "The phase diagram of water and the magnetic fields of Uranus and Neptune," Icarus **211**, 798 (2011).

[9] S. Stanley and J. Bloxham, "Convective-region geometry as the cause of Uranus' and Neptune's unusual magnetic fields," Nature **428**, 151 (2004).

[10] S. Stanley and J. Bloxham, "Numerical dynamo models of Uranus' and Neptune's magnetic fields," Icarus **184**, 556 (2006).

[11] D. Kraus, J. Vorberger, A. Pak, N. Hartley, L. Fletcher, S. Frydrych, E. Galtier, E. Gamboa, D. Gericke, S. Glenzer, E. Granados, M. MacDonald, A. MacKinnon, E. McBride, I. Nam, P. Neumayer, M. Roth, A. Saunders, A. Schuster, P. Sun, T. V. Driel, T. Döppner, and R. Falcone, "Formation of diamonds in laser-compressed hydrocarbons at planetary interior conditions," Nat. Astron **9**, 606 (2017).

[12] N. F. Ness, M. H. Acuña, K. W. Behannon, L. F. Burlaga, J. E. P. Connerney, R. P. Lepping, and F. M. Neubauer, "Magnetic fields at uranus," Science **233**, 85–89 (1986).

[13] M. French, T. R. Mattsson, N. Nettelmann, and R. Redmer, "Equation of state and phase diagram of water at ultrahigh pressures as in planetary interiors," Phys. Rev. B **79**, 054107 (2009).

[14] P. Sperling, E. J. Gamboa, H. J. Lee, H. K. Chung, E. Galtier, Y. Omarbakiyeva, H. Reinholz, G. Röpke, U. Zastrau, J. Hastings, L. B. Fletcher, and S. H. Glenzer, "Free-Electron X-Ray Laser Measurements of Collisional-Damped Plasmons in Isochorically Heated Warm Dense Matter," Phys. Rev. Lett. **115** (2015).

[15] B. Witte, L. Fletcher, E. Galtier, E. Gamboa, H. Lee, U. Zastrau, R. Redmer, S. Glenzer, and P. Sperling, "Warm dense matter demonstrating non-drude conductivity from observations of nonlinear plasmon damping," Phys. Rev. Lett. **118**, 225001 (2017).

[16] B. B. Witte, G. Röpke, P. Neumayer, M. French, P. Sperling, V. Recoules, S. H. Glenzer, and R. Redmer, "Comment on "isochoric, isobaric, and ultrafast conductivities of aluminum, lithium, and carbon in the warm dense matter regime"," Phys. Rev. E **99**, 047201 (2019).

[17] S. Frydrych, J. Vorberger, N. J. Hartley, A. K. Schuster, K. Ramakrishna, A. M. Saunders, T. van Driel, R. W. Falcone, L. B. Fletcher, E. Galtier, E. J. Gamboa, S. H. Glenzer, E. Granados, M. J. MacDonald, A. J. MacKinnon, E. E. McBride, I. Nam, P. Neumayer, A. Pak, K. Voigt, M. Roth, P. Sun, D. O. Gericke, T. Döppner, and D. Kraus, "Demonstration of X-ray Thomson scattering as diagnostics for miscibility in warm dense matter," Nature Communications **11**, 2620 (2020).

[18] P. M. Celliers, G. W. Collins, D. G. Hicks, M. Koenig, E. Henry, A. Benuzzi-Mounaix, D. Batani, D. K. Bradley, L. B. Da Silva, R. J. Wallace, S. J. Moon, J. H. Eggert, K. K. Lee, L. R. Benedetti, R. Jeanloz, I. Masclet, N. Dague, B. Marchet, M. Rabec, L. Gloahec, C. Reverdin, J. Pasley, O. Willi, D. Neely, and C. Danson, "Electronic conduction in shock-compressed water," Phys. Plasma **11**, L41 (2004).

[19] M. D. Knudson, M. P. Desjarlais, R. W. Lemke, T. R. Mattsson, M. French, N. Nettelmann, and R. Redmer, "Probing the Interiors of the Ice Giants: Shock Compression of Water to 700 GPa and 3.8 g/cm^3," Phys. Rev. Lett. **108**, 091102 (2012).

[20] T. Kimura, N. Ozaki, T. Sano, T. Okuchi, T. Sano, K. Shimizu, K. Miyanishi, T. Terai, T. Kakeshita, Y. Sakawa, and R. Kodama, "P - ρ - T measurements of H2O up to 260 GPa under laser-driven shock loading," J. Chem. Phys. **142**, 164504 (2015).

[21] M. Millot, S. Hamel, J. Rygg, P. Cellier, G. Collins, F. Coppari, D. Fratanduono, R. Jeanloz, D. Swift, and J. Eggert, "Experimental evidence for superionic water ice using shock compression," Nat. Phys. **14**, 297 (2018).

[22] C. A. Stan, D. Milathianaki, H. Laksmono, R. G. Sierra, T. A. McQueen, M. Messerschmidt, G. J. Williams, J. E. Koglin, T. J. Lane, M. J. Hayes, S. A. Guillet, M. Liang, A. L. Aquila, P. R. Willmott, J. S. Robinson, K. L. Gumerlock, S. Botha, K. Nass, I. Schlichting, R. L. Shoeman, H. A. Stone, and S. Boutet, "Liquid explosions induced by X-ray laser pulses," Nat. Phys. **12**, 966 (2016).

[23] S. H. Glenzer, L. B. Fletcher, E. Galtier, B. Nagler, R. Alonso-Mori, B. Barbrel, S. B. Brown, D. A. Chapman, Z. Chen, C. B. Curry, F. Fiuza, E. Gamboa, M. Gauthier, D. O. Gericke, A. Gleason, S. Goede, E. Granados, P. Heimann, J. Kim, D. Kraus, M. J. MacDonald, A. J. MacKinnon, R. Mishra, A. Ravasio, C. Roedel, P. Sperling, W. Schumaker, Y. Y. Tsui, J. Vorberger, U. Zastrau, A. Fry, W. E. White, J. B. Hasting, and H. J. Lee, "Matter under extreme conditions experiments at the Linac Coherent Light Source," J. Phys. B At. Mol. Opt. Phys. **49**, 092001 (2016).

[24] "Structure retrieval in liquid-phase electron scattering," Phys. Chem. Chem. Phys. **1** (2020).

[25] T. Gorkhover, A. Ulmer, K. Ferguson, M. Bucher, F. R. Maia, J. Bielecki, T. Ekeberg, M. F. Hantke, B. J. Daurer, C. Nettelblad, J. Andreasson, A. Barty, P. Bruza, S. Carron, D. Hasse, J. Krzywinski, D. S. Larsson, A. Morgan, K. Mühlig, M. Müller, K. Okamoto, A. Pietrini, D. Rupp, M. Sauppe, G. Van Der Schot, M. Seibert, J. A. Sellberg, M. Svenda, M. Swiggers, N. Timneanu, D. Westphal, G. Williams, A. Zani, H. N. Chapman, G. Faigel, T. Möller, J. Hajdu, and C. Bostedt, "Femtosecond X-ray Fourier holography imaging of free-flying nanoparticles," Nat. Photonics **12**, 150 (2018).

[26] N. W. Ashcroft and N. D. Mermin, *Solid State Physics* (Harcourt Brace Jovanovich Publishers, Toronto, 1976).

[27] K. R. Beyerlein, H. O. Jönsson, R. Alonso-Mori, A. Aquila, S. Bajt, A. Barty, R. Bean, J. E. Koglin, M. Messerschmidt, D. Ragazzon, D. Sokaras, G. J. Williams, S. Hau-Riege, S. Boutet, H. N. Chapman, N. Tîmneanu, and C. Caleman, "Ultrafast nonthermal heating of water initiated by an X-ray Free-Electron Laser," Proceedings of the National Academy of Sciences **6**, 201711220 (2018).

[28] A. Ng, P. Sterne, S. Hansen, and V. t. Recoules, "dc conductivity of two-temperature warm dense gold," Phys. Rev. E **94**, 033213 (2016).

[29]Z. Chen, B. Holst, S. Kirkwood, V. Sametoglu, M. Reid, Y. Tsui, V. Recoules, and A. Ng, "Evolution of ac conductivity in nonequilibrium warm dense gold," Phys. Rev. Lett. **110**, 135001 (2013).

[30]K. Widmann and *et al.*, "Single-state measurement of electrical conductivity of warm dense gold," Phys. Rev. Lett. **92**, 125002 (2004).

[31]J. Koralek, J. Kim, P. Bruza, C. B. Curry, Z. Chen, and *et al*., "Generation and characterization of ultrathin free-flowing liquid sheets," Nat. Comm **9**, 1353 (2018).

[32]V. Svoboda, R. Michiels, A. LaForge, J. Med, F. Stienkemeier, P. Slavicek, and H. Wörner, "Real-time observation of water radiolysis and hydrated electron formation induced by extreme-ultraviolet pulses," Sci. Adv **6**, eaaz0385 (2020).

[33]R. Matula, "Electrical resistivity of copper, gold, palladium, and silver," J. Phys. Chem. Ref. Data **8**, 1147 (1979).

[34]J. M. Ziman, "A theory of the electrical properties of liquid metals. i: The monovalent metals," Philos. Mag. **6**, 1013 (1961).

[35]M. Born and E. Wolf, *Principles of Optics, 6th ed.,* (Pergamon Press, Oxford, 1980).

[36]K. Tiedtke, A. Azima, N. von Bargen, L. Bittner, S. Bonfigt, and *et al*., "The soft x-ray free-electron laser flash at desy: beamlines, diagnostics and end-stations," New J. Phys. **11**, 023029 (2009).

[37]B. Henke, E. Gullikson, and J. Davis, "X-ray interactions: photoabsorption, scattering, transmission, and reflection at e=50-30000 ev, z=1-92," At. Data Nucl. Data Tables **54**, 181 (1993).

[38]R. Garcia-Molina, I. Abril, I. Kyriakou, and D. Emfietzoglou, "Inelastic scattering and energy loss of swift electron beams in biologically relevant materials," Surf. Interface Anal. **49**, 11 (2017).

[39]U. Zastrau, P. Sperling, A. Becker, T. Bornath, R. Bredow, T. Döppner, S. Dziarzhytski, T. Fennel, L. B. Fletcher, E. Förster, C. Fortmann, S. H. Glenzer, S. Göde, G. Gregori, M. Harmand, V. Hilbert, B. Holst, T. Laarmann, H. J. Lee, T. Ma, J. P. Mithen, R. Mitzner, C. D. Murphy, M. Nakatsutsumi, P. Neumayer, A. Przystawik, S. Roling, M. Schulz, B. Siemer, S. Skruszewicz, J. Tiggesbäumker, S. Toleikis, T. Tschentscher, T. White, M. Wöstmann, H. Zacharias, and R. Redmer, "Equilibration dynamics and conductivity of warm dense hydrogen," Phys. Rev. E - Stat. Nonlinear, Soft Matter Phys. **90**, 013104 (2014).

[40]U. Zastrau, P. Sperling, M. Harmand, A. Becker, T. Bornath, R. Bredow, S. Dziarzhytski, T. Fennel, L. B. Fletcher, E. Förster, S. Göde, G. Gregori, V. Hilbert, D. Hochhaus, B. Holst, T. Laarmann, H. J. Lee, T. Ma, J. P. Mithen, R. Mitzner, C. D. Murphy, M. Nakatsutsumi, P. Neumayer, A. Przystawik, S. Roling, M. Schulz, B. Siemer, S. Skruszewicz, J. Tiggesbäumker, S. Toleikis, T. Tschentscher, T. White, M. Wöstmann, H. Zacharias, T. Döppner, S. H. Glenzer, and R. Redmer, "Resolving ultrafast heating of dense cryogenic hydrogen," Phys. Rev. Lett. **112**, 105002 (2014).

[41]U. Samir, K. H. Wright, and N. H. Stone, "The expansion of a plasma into a vacuum: Basic phenomena and processes and applications to space plasma physics," Rev. Geophys. **21**, 1631 (1983).

[42]Z. Chen, M. Mo, L. Soulard, V. Recoules, P. Hering, Y. Y. Tsui, S. H. Glenzer, and A. Ng, "Interatomic Potential in the Nonequilibrium Warm Dense Matter Regime," Phys. Rev. Lett. **121**, 075002 (2018).

[43]W. Southwell, "Gradient-index antireflection coatings," Opt. Lett. **8**, 584 (1984).

[44]D. Fisher, M. Fraenkel, Z. Henis, E. Moshe, and S. Eliezer, "Interband and intraband (drude) contributions to femtosecond laser absorption in aluminum," Phys. Rev. E **65**, 016409 (2001).

[45]M. French and R. Redmer, "Electronic transport in partially ionized water plasmas," Phys. Plasmas **24**, 092306 (2017).

[46]R. Scipioni, L. Stixrude, and M.P.Desjarlais, "Electrical conductivity of sio2 at extreme conditions and planetary dynamos," Proc. Natl. Acad. Sci. U.S.A. **114**, 9009 (2017).

[47]G. Kresse and J. Hafner, "Ab initio molecular dynamics for liquid metals," Phys. Rev. B **47**, 558–561 (1993).

[48]G. Kresse and J. Hafner, "Ab initio molecular dynamics for open-shell transition metals," Phys. Rev. B **48**, 13115–13118 (1993).

[49]G. Kresse and J. Hafner, "Ab initio molecular-dynamics simulation of the liquid-metal-amorphous-semiconductor transition in germanium," Phys. Rev. B **49**, 14251–14269 (1994).

[50]G. Kresse and J. Furthmüller, "Efficient iterative schemes for ab initio total-energy calculations using a plane-wave basis set," Phys. Rev. B **54**, 11169–11186 (1996).

[51]J. P. Perdew, K. Burke, and M. Ernzerhof, "Generalized gradient approximation made simple," Phys. Rev. Lett. **77**, 3865–3868 (1996).

[52]M. French, T. R. Mattsson, N. Nettelmann, and R. Redmer, "Equation of state and phase diagram of water at ultrahigh pressures as in planetary interiors," Phys. Rev. B **79**, 054107 (2009).

[53]M. French, T. R. Mattsson, and R. Redmer, "Diffusion and electrical conductivity in water at ultrahigh pressures," Phys. Rev. B **82**, 174108 (2010).

[54]M. Gajdoš, K. Hummer, G. Kresse, J. Furthmüller, and F. Bechstedt, "Linear optical properties in the projector-augmented wave methodology," Phys. Rev. B **73**, 045112 (2006).

[55]R. Kubo, "Statistical-Mechanical Theory of Irreversible Processes. I. General Theory and Simple Applications to Magnetic and Conduction Problems," J. Phys. Soc. Jpn. **12**, 570 (1957).

[56]D. A. Greenwood, "The boltzmann equation in the theory of electrical conduction in metals," Proc. Phys. Soc. **71**, 585–596 (1958).

[57]J. Heyd, G. E. Scuseria, and M. Ernzerhof, "Erratum: "hybrid functionals based on a screened coulomb potential" [j. chem. phys. [bold 118], 8207 (2003)]," J. Chem. Phys. **124**, 219906 (2006).

[58]M. French and R. Redmer, "Optical properties of water at high temperature," Phys. Plasmas **18**, 043301 (2011).

[59]A. Ravasio, M. Bethkenhagen, J.-A. Hernandez, A. Benuzzi-Mounaix, F. Datchi, M. French, M. Guarguaglini, F. Lefevre, S. Ninet, R. Redmer, and T. Vinci, "Metallization of shock-compressed liquid ammonia," Phys. Rev. Lett. **0**, accepted (2020).

[60]B. Holst, V. Recoules, S. Mazevet, M. Torrent, A. Ng, S. Kirkwood, V. Sametoglu, M. Reid, and Y. Y. Tsui, "An ab-initio model on optical properties of non-equilibrium Warm Dense Matter," **90**, 035121 (2014).

[61]D. Kremp, M. Schlanges, and W.-D. Kraeft, *Quantum Statistics of Non-ideal Plasmas* (Springer, Berlin, Heidelberg, 2005).

[62]S. Glenzer and R. Redmer, "X-ray thomson scattering in high energy density plasmas," Rev. Mod. Phys. **81**, 1625 (2009).

[63]J. L. F. Abascal and C. Vega, "A general purpose model for the condensed phases of water: Tip4p/2005," J. Chem. Phys. **123**, 234505 (2005).

[64]G. Hura, J. M. Sorenson, R. M. Glaeser, and T. Head-Gordon, "High-quality x-ray scattering experiment on liquid water at ambient conditions," J. Chem. Phys. **113**, 9140 (2000).